Characterization of the detection chain of the Micro-channel X-ray Telescope

Francesco Ceraudo, Aline Meuris, Eric Doumayrou, Luc Dumaye, Alain Goetschy, Tony Lavanant, Michel Lortholary, Isabelle Le Mer, François Nico, Frédéric Pinsard, et al.

Version of Record: https://www.sciencedirect.com/science/article/pii/S016890022030560X
Manuscript_ec99a38d406162e95f321d2529217990

Characterization of the detection chain of the Micro-channel X-ray Telescope

Francesco Ceraudo[a,1,*], Aline Meuris[a], Eric Doumayrou[a], Luc Dumaye[a], Alain Goetschy[a], Tony Lavanant[a], Michel Lortholary[a], Isabelle Le Mer[a], François Nico[a], Frédéric Pinsard[a], Marin Prieur[a], Diana Renaud[a], Benjamin Schneider[a], Thierry Tourrette[a], François Visticot[a], Norbert Meidinger[b], Danilo Mießner[c], Diego Götz[a]

[a] *Astrophysics Division, IRFU, AIM, CEA, CNRS, Université Paris-Saclay, Université Paris Diderot, Sorbonne Paris Cité, F-91191, Gif-sur-Yvette, France*
[b] *Max-Planck-Institut für extraterrestrische Physik, Giessenbachstrasse, 85748 Garching, Germany*
[c] *Halbleiterlabor der Max-Planck Gesellschaft, Otto-Hahn-Ring 6, 81739 München, Germany*

Abstract

This paper describes the first performance tests and characterization of the detection chain of the Micro-channel X-ray Telescope (MXT), one of the instruments on board the French-Chinese mission SVOM for the study of Gamma-Ray Bursts. The MXT detector consists of a back-illuminated 450 µm-thick fully-depleted frame-store silicon pnCCD, operating in the $0.2-10$ keV energy range. Featuring an imaging area of $\approx 4\,\mathrm{cm}^2$, the device is read out in parallel by two CAMEX ASICs and is powered and controlled by its dedicated Front-End Electronics. A complete setup based on a cryostat and a multi-energy X-ray source have been designed for the characterization of the detection chain. The tests, performed at $\approx -65\,^{\circ}\mathrm{C}$, demonstrate a spectral resolution of (82 ± 2) eV at 1.5 keV as well as a < 200 eV low-level threshold. Both of those results are in compliance with the performance requirements of the instrument.

*Corresponding author
Email address: francesco.ceraudo@cea.fr, francesco.ceraudo@inaf.it (Francesco Ceraudo)
[1]Present address: Institute for Space Astrophysics and Planetology, National Institute for Astrophysics, Via del Fosso del Cavaliere 100, 00133, Roma, Italy

Keywords:
SVOM, MXT, pnCCD, X-ray Spectroscopy, Space Instrumentation

1. Introduction

The *Space-based multi-band astronomical Variable Object Monitor* (SVOM) is a Chinese-French space astronomy mission for the study of Gamma-Ray Bursts (GRBs) and other transient astrophysical phenomena [1]. To be launched at the end of 2021, SVOM will achieve high sensitivity from MeV photons to Near Infra-Red wavelengths. This will allow the detection of all types of GRBs, for which it will provide fast and reliable positions as well as spectral and temporal evolution.

Part of the French contribution to the scientific payload of the satellite, the *Micro-channel X-ray Telescope* or MXT [2], depicted in Fig. 1, will be the first instrument for space astronomy to mount Micro-Pore Optics (MPOs) arranged in a *lobster-eye* configuration. The optics have been developed and built by the University of Leicester, using MPO plates from Photonis France [3]. With a 1.15 m focal length, the telescope will operate in the $0.2 - 10$ keV range and feature a 10 arcmin angular resolution along with an effective area of 23 cm^2 at 1 keV. MXT will have a twofold goal: (1) to provide < 2 arcmin source localization accuracy in less than 10 min for $> 90\,\%$ of GRBs; (2) to study the afterglow emission with an energy resolution of ~ 80 eV at 1.5 keV.

To ensure its objectives, the focal plane of MXT will be equipped with a 450 µm-thick fully-depleted frame-store Charge-Coupled Device entirely based on pn-junctions (pnCCD). Heritage of XMM/EPIC-pn [4] and provided by the Max Planck Institute for Extraterrestrial Physics (MPE), it was originally developed as one of the earlier detector models for the eROSITA mission [5]. Composed of a matrix of 256×256 75 µm-side pixels, the pnCCD is read out by two CAMEX 128MJD ASICs (ENC $\approx 2\,\mathrm{e}^-_{\mathrm{rms}}$) [6, 7]. The device is visible in Fig. 1c.

MXT will be the first experiment to operate a pnCCD in the harsh environment of Low-Earth Orbit. This presents a highly variable thermal radiative background, dominated by periodic occultations and Earth's infrared and albedo emissions. In addition, the orbit features intense particle radiation, due to the fact that the SVOM satellite will cross several times per day the South Atlantic Anomaly, a region with high concentration of protons and electrons trapped in the Earth's magnetic field. The design of MXT is

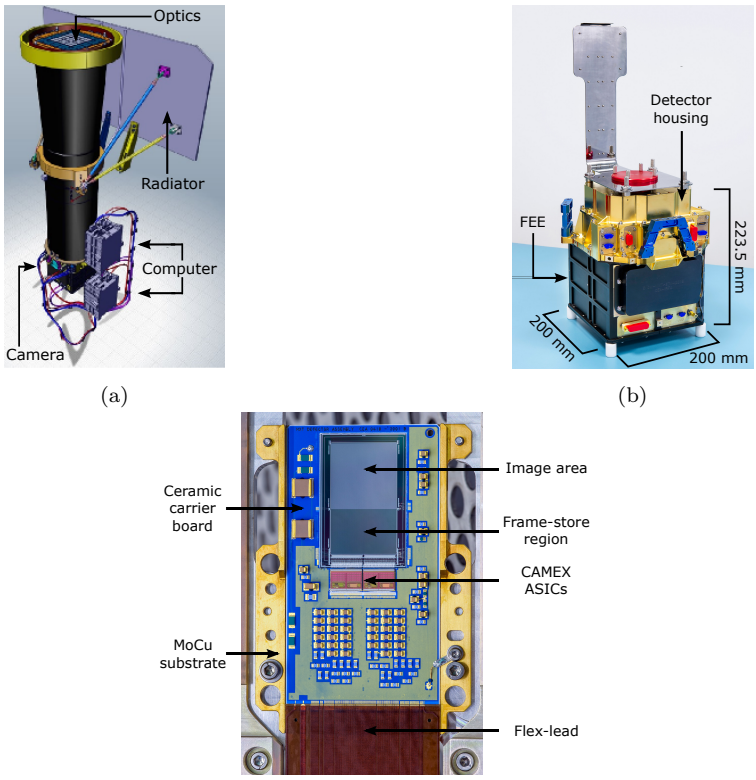

Figure 1: The Micro-channel X-ray Telescope (MXT). a) Overview of the telescope. b) The MXT camera, housing the detector and the Front-End Electronics box. c) Close-up of the front-side of the MXT detector mounted on its carrier board: its working principle and main components are detailed in § 2.

further affected by its mass (35 kg) and power (50 W) budgets, very tight when compared to instruments with similar purposes such as SWIFT/XRT, with its mass of ≈ 200 kg [8]. All those constraints force the MXT detector to function at $\approx -65\,^{\circ}$C, a far higher temperature than the $-90\,^{\circ}$C of missions such as XMM/EPIC-pn and eROSITA, both of which use similar pnCCDs. It is therefore mandatory to study the spectral performances of the MXT detector and to verify the compliance with the scientific requirements, i.e. energy resolution of ~ 80 eV at 1.5 keV and low-energy threshold of 200 eV.

The following sections present an overview of the working principle of the MXT detector and the subsystems allowing its operation (§ 2). Afterwards, the analysis algorithms of the data of the MXT pnCCD are detailed (§ 3). Finally, the tests and results carried out on the Performance Model of the MXT detector are discussed (§ 4).

2. MXT detection chain

2.1. The MXT detector

By taking advantage of the principle of sidewards depletion [9], the application of a set of voltages to the electrodes (cathodes) at the front and back sides of the detector allows the silicon bulk of the MXT Charge Coupled Device to be depleted over its entire 450 µm-thickness. Full depletion and back-illumination grant the sensor a $> 90\,\%$ quantum efficiency over the $1 - 10$ keV range. Featuring a monolithic back-side also ensures a 100 % fill factor. The front-side of the detector is segmented into electrodes (called shift registers or phases) grouped into a matrix of pixels. Two active regions can be identified (whose purpose is defined below): an *image area*, made out of 256×256 pixels measuring 75 µm $\times$ 75 µm (active area of 19.2 mm $\times$ 19.2 mm), and a *frame-store region*, having 256×256 pixels measuring 75 µm $\times$ 51 µm.

2.2. Acquisition and readout

During the integration phase (lasting $t_{\mathrm{int}} = 100$ ms in MXT), the image region of the detector is exposed to X-rays which enter from the back-side and deposit their energy via photoelectric effect creating electron-hole clouds. While holes are absorbed by the cathodes, electrons migrate to local potential minima under the pixels near the front-side of the pnCCD. The charges thus distributed below the pixels of the matrix collectively make up a *frame*. After integration, periodic changes of the electrical potential of the shift registers allow the charge packets to be moved pixel by pixel towards the bottom of the

image area and into the frame-store region, which is shielded against X-rays, where they await readout. The frame shift takes $t_{\mathrm{transf}} = 230\,\mu\mathrm{s}$ in MXT, thus reducing the probability of out-time-events[2] to $t_{\mathrm{int}}/t_{\mathrm{transf}} \approx 0.2\,\%$. The readout process occurs in 10 ms in a *column-parallel* fashion, meaning that no pixel serialization is present, but each CCD column is provided with its own anode and connected to one input channel of the two CAMEX ASICs (Fig. 1c). Both the pnCCD and the two CAMEX are mounted on an alumina (Al_2O_3) carrier board coupled with a copper-molybdenum (MoCu) substrate and kept at the nominal operating temperature of $\approx -65\,^{\circ}\mathrm{C}$ by an active cooling system made out of three Thermo-Electric Coolers (TECs).

2.3. Front-End Electronics

A warm Front-End Electronics (FEE, Fig. 1b) ensures: (1) power supply of the focal plane and analog-to-digital conversion of the CAMEX output; (2) readout clocks and sequencing; (3) on-line pre-processing for photon extraction and communication with the on-board computer (the MXT Data Processing Unit or MDPU). Two modes of operation are possible: (1) in *full-frame mode* whole 256×256-pixel frames exit the FEE without treatment; in *event mode* the FEE output consists of a stream of hit pixels extracted via on-line pre-processing by the electronics itself (algorithms are detailed in § 3). Due to the performance limitations of the ATMEL FPGA on the FEE, the frequency of the Spacewire link is limited to 20 MHz, which requires to slow down the data transfer rate in full frame mode, and is achieved by increasing the integration time to 200 ms ($5\,\mathrm{frame\,s^{-1}}$). On the contrary, in event mode the nominal 100 ms ($10\,\mathrm{frame\,s^{-1}}$) exposure time can be respected, with an output of up to 5000 hit pixels per frame.

3. Analysis algorithms

Written entirely in Python 3.7, the algorithms for image and spectral analysis follow the same logic as those developed by the MPE for the characterization of the eROSITA detector [10]. Nonetheless, the codes have been

[2] Out-time-events are photons recorded when the charges are being shifted towards the anodes: their arrival positions are not correctly measured and they cause trails in the image along the transfer direction.

improved to enhance robustness to outliers and execution speed, most notably via the implementation of a multi-threading mode of execution whenever possible.

The algorithms require two kinds of frames: *dark frames*, i.e. images in which the detector has not been exposed to X-rays, and *photon frames* in which the X-ray source is present. Before energy calibration is performed (to be described in § 3.3), all data are to be considered in analog-to-digital units (ADU).

Frame reduction is performed completely off line in full-frame mode (§ 2.3). In event mode, only photon extraction (§ 3.2) is carried out during the acquisition and it requires offset (§ 3.1) and threshold (§ 3.2) maps to be calculated off line and then loaded into the FEE. In every case, the spectral analysis takes place after all the data have been gathered. As a reference, in space, both offset and threshold maps will be computed on board and uploaded by the MXT Data Processing Unit.

3.1. Dark frame reduction

The voltages of the analog channels of the readout electronics determine an image-wide offset that must be subtracted[3]. Given a succession of dark frames S, so that a pixel at row i and column j on frame k may be identified as S_{ijk}, the *offset map* O is defined as the pixel-by-pixel median along the temporal direction:

$$O_{ij} = [S_{ijk}]_k^{50\,\%}\,, \tag{1}$$

where $[\cdot]_k^{50\,\%}$ represents the median along the time axis, i.e. frame number, as frames are acquired sequentially. It is worth noting that the median has an important advantage over, say, the mean, as it is more robust against outliers, e.g. cosmic ray traces in the dark frames.

Due to the CCD's parallel readout (§ 2.2), fluctuations in the references of the analog inputs affect all the pixels in a row, while varying from row to row. This phenomenon is called *common-mode noise* CM and quantified as the median along each CCD row of an offset-subtracted frame:

$$\mathrm{CM}_{ik} = [S_{ijk} - O_{ij}]_j^{50\,\%}\,, \tag{2}$$

[3]In the case at hand, the leakage current of the detector is so low that its build-up in the CCD pixels is a negligible contribution to the offset when compared to the analog channels.

where the notation retains its meaning from eq. (1). It is worth noting that the common-mode noise is derived separately for the two CAMEX, i.e. two medians are calculated per row, each one over 128 pixels. Failing to take this noise source into account may negatively affect the spectroscopic performances of the detector.

After the correction of both offset and common mode, a frame is referred to as a *flat frame* F:

$$F_{ijk} = S_{ijk} - O_{ij} - \mathrm{CM}_{ik}. \tag{3}$$

Finally, the *noise map* N is taken as the pixel-by-pixel difference between the 84.13 %-percentile and the median (which should be zero after all the corrections) of the distribution of counts along the time axis of a succession of flat dark frames[4]:

$$N_{ij} = [F_{ijk}]_k^{84.13\,\%-50\,\%}. \tag{4}$$

This approach retains the robustness to outliers of the median while at the same time staying well defined even in case of an asymmetric and/or non-Gaussian distribution, unlike other estimators such as the standard deviation.

3.2. Photon frame reduction

Flat photon frames F are obtained by applying eq. (3) to photon frames S, with the offset map O resulting from the analysis of dark frames and the common-mode CM from the offset-subtracted photons frames themselves according to eq. (2). The pixels are then compared to the noise level by applying a *threshold map* T equal to a multiple of the noise map N, i.e. $T = nN$. A pixel in position (i, j) on frame k is therefore considered to be *hit* if

$$F_{ijk} > T_{ij}. \tag{5}$$

The value of $n = 4$ is used hereafter, as tests carried out by the MXT team have verified it ensures the best spectral resolution in the case under study. This algorithm mimics the operations of the FEE in event mode and is thus representative within the wider scope of the instrument performances. The main difference between the two processes is the method by which common-mode noise is estimated, which is implemented in an approximated form in the FEE due to performance limitations of the available FPGA.

[4]The values of 84.13 % is chosen to match the standard deviation in case of a symmetric Gaussian. Indeed, given a Gaussian distribution of mean μ and standard deviation σ, the integral from $-\infty$ to $\mu + \sigma$ equals 0.8413.

As a last step, a pattern-recognition routine groups neighboring pixels sharing at least one side and classifies them according to the XMM/EPIC convention for photon and non-photon events (this is done off line regardless of the mode of operation). As a matter of fact, photons create spherical charge clouds of dimensions smaller than (but still comparable to) the pixels and therefore can be collected by up to four pixels arranged in a square, implying that only certain configurations can be accepted as results of photon interactions. Customarily, photon events are referred to by their multiplicity, i.e. the number of pixels among which the signal is shared, hence one considers single, double, triple or quadruple events.

3.3. Energy calibration

Since each CCD column is provided with its own analog channel, energy calibration must be performed column-wise. Single events are sorted according to the readout channel and 256 uncalibrated spectra are thus calculated. If necessary an additional low-energy threshold (*spectral threshold*) may be applied to the spectra, a functionality that is found also in the final flight configuration, where the MDPU can add a second threshold to the one used for event extraction by the FEE, i.e. the *extraction threshold* of eq. (5).

Gaussian profiles are then fitted to some reference peaks of the column-by-column spectra and a linear calibration is performed for each CCD channel. Both a gain and an offset are calculated, the second one being supposedly zero, unless non-linear effects are present.

3.4. CTI correction

As electron packets are transferred towards the anodes for readout, a fraction of the charge may be left behind: this phenomenon is described by the *Charge Transfer Inefficiency* CTI or its complement the *Charge Transfer Efficiency* CTE = 1−CTI. CTI affects pixels more as the number of transfers increases. To correct for this effect, after energy calibration, single events are grouped according to the CCD row and 256 row-by-row spectra are thus calculated. Line profiles are fitted similarly to the previous case. Here, however, the centers of the reference lines are then considered as a function of the number of transfers and the following function is fitted

$$E_n = E_0 \mathrm{CTE}^n, \tag{6}$$

where E_n is the line center after n transfers, E_0 is left as a free parameter and CTE is the Charge Transfer Efficiency. After the estimation of the CTE,

Table 1: Composition of the fluorescence target and corresponding relevant spectral lines. Precise percentages of the materials are not known and optimization of the line intensities is completely empirical.

Element	Spectral line eV	
Al	1486	
Sn	3443	3772
Ti	4509	4932
Cr	5412	5947
Fe	6395	7058
Ni	7472	
Cu	8040	8905

the pixel amplitude A_{ij} in ADU or keV may be corrected for this effect by putting

$$A'_{ij} = \frac{A_{ij}}{\frac{E_0}{E_\gamma}\mathrm{CTE}\,(E_\gamma)^{n_i}}, \tag{7}$$

where n_i is the number of transfers corresponding to the i-th row and E_γ is the *true* photon energy at which the CTE, which is itself energy dependent, is calculated.

3.5. Iterative approach

If the CTI is not properly accounted for, the gain estimation will be slightly off, which in turn affects the determination of the CTI. This is tackled with an iterative approach. ADU values are energy-calibrated and employed to evaluate the CTE, which is used to correct the original ADU data and allow for a better calibration. After that, a new *relative* estimate of the CTE is derived, i.e. from already CTI-corrected data, and used again to correct the original measurements. The procedure is repeated until a satisfying level of precision is reached: in practice a couple of repetitions ensure that the variation of the fitting parameters between iterations stays below the uncertainty of the fit.

4. Results

In the following, the results of the laboratory tests carried out on the Performance Model of the MXT detector are presented. The device is tested

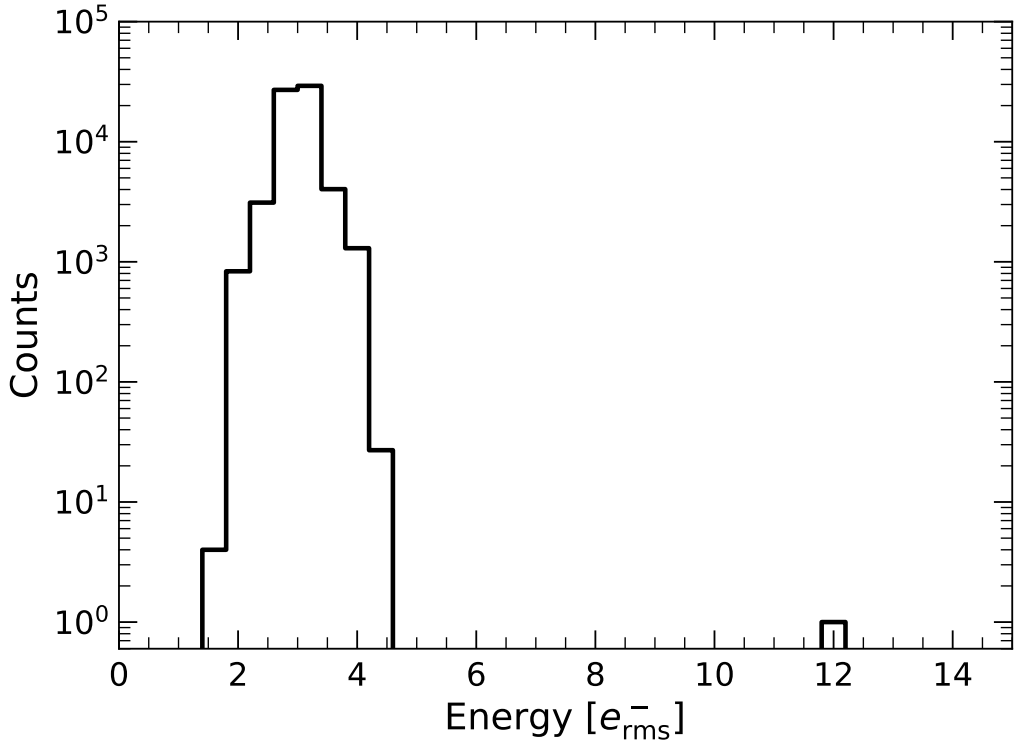

Figure 2: Histogram of the noise values. A median value of $3.25\,e^-_{rms}$ (47 eV) is measured, with 99.73 % (i.e. 3σ-limit) of pixels below $4.10\,e^-_{rms}$ (60 eV). A single noisy pixel is detected.

in a dedicated cryostat and photons are generated via an X-ray tube illuminating a composite fluorescent target, whose materials are chosen to generate a series of spectral lines sampling much of the energy range of operation of MXT (Tab. 1). A residual Bremsstrahlung emission is also present in the spectrum.

All measurements are taken at a temperature of $\approx -65\,^{\circ}$C, representative of in-orbit thermal conditions. In line with the flight configuration, the FEE is kept at room temperature outside the cryostat. Both full-frame and event modes of operation are tested and, unless otherwise specified, the following considerations and comments apply to both.

4.1. Noise

Fig. 2 shows the histogram of the pixels of the noise map. The noise is uniform across the detector with a median of $3.2\,\mathrm{e^-_{rms}}$ and 99.73 % (i.e. 3σ-limit) of pixels below $4.1\,\mathrm{e^-_{rms}}$. A single isolated bright spot near the center of the CCD is measured, whose associated noise is $12.3\,\mathrm{e^-_{rms}}$. This is is likely due to a defect on the detector itself and can be safely flagged and ignored in the analysis.

If the spectral calibration of the chain is considered (to be discussed below), the figures above translate to an average pixel-by-pixel threshold of 47 eV, with a 99.73 % upper limit at $\approx 60\,\mathrm{eV}$. This is fully compatible with the 200 eV requirement on the low-energy threshold of MXT.

4.2. Intensity map

Fig. 3 shows the cumulative map of the photons detected over 2000 frames over the entire energy range generated by the X-ray tube. The response is uniform across the whole detector.

4.3. Energy resolution

Examples of the detector-wide spectra obtained using single events, double events whichever the orientation, and all events regardless of the multiplicity are shown in Fig. 4.

To calibrate single-event spectra, a model consisting of five Gaussian line profiles and a fourth-degree polynomial continuum is fitted on each column-wise and row-wise spectrum. This allows to achieve better estimation of both line centers and widths by taking into account deformations resulting from the continuous Bremsstrahlung emission of the X-ray generator.

Higher multiplicity spectra are calibrated and corrected by using CTI and spectral gain and offset estimated from single events. The spectra are then shifted by an energy-independent offset to align them with respect to the spectrum of single events. This procedure is performed to compensate for a multiplicity-dependent energy shift already observed in XMM/EPIC-pn and similarly addressed [11]. Applying the shift allows to improve the energy resolution of the spectrum of all events by $\approx 20\,\%$, so that the dominant remaining noise contribution is electronic noise. This approach to calibration is preferred to employing the same algorithm used for singles to all multiplicities because it entails a smaller number of calibration parameters, i.e. energy-dependent CTE, 256 column-wise gains, 256 column-wise offsets and

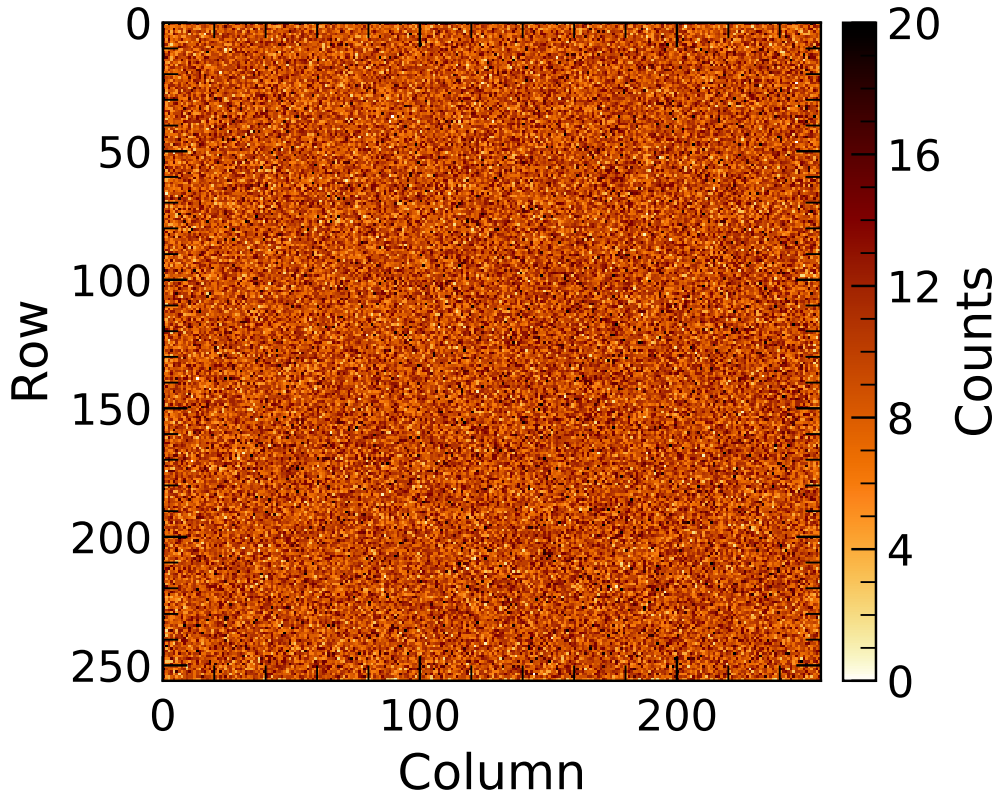

Figure 3: Cumulative map of the photons detected over 2000 frames. The response appear to be uniform across the device.

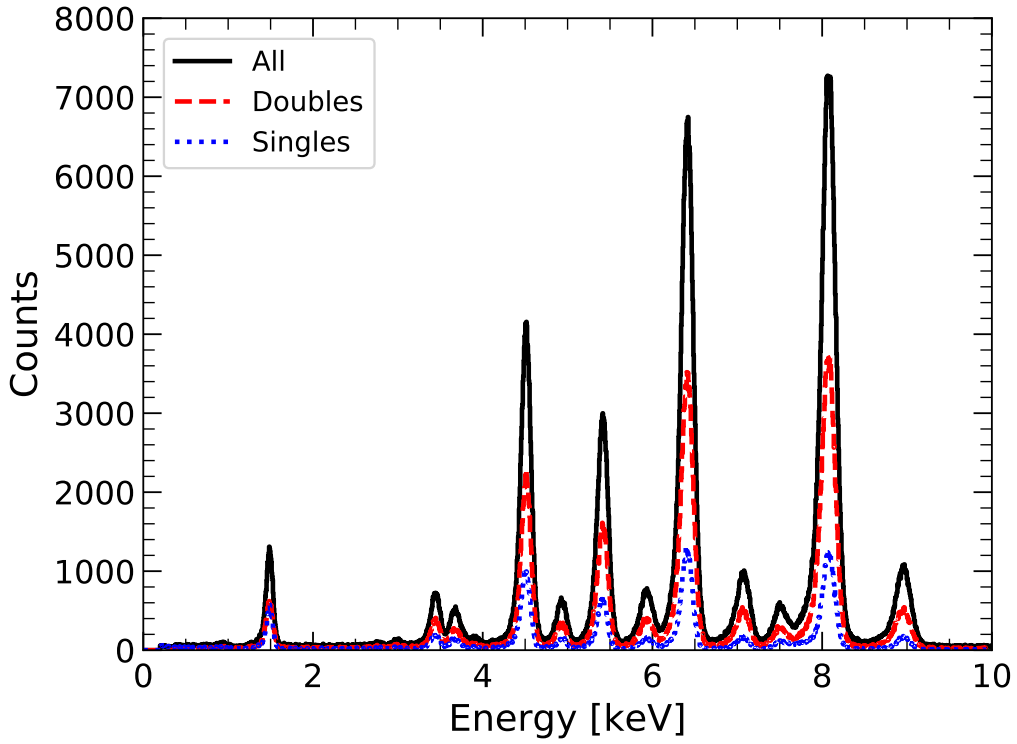

Figure 4: Spectrum of single, double and all events. The reader is referred to Tab. 1 for an identification of the spectral features, and to Tab. 2 and 3 for the values of the spectral resolution at the five most prominent lines.

Table 2: Measured energy resolution for single and all events in full-frame mode.

Line	Energy eV	FWHM eV	
		Singles	All
Al-K_α	1486	82 ± 2	91 ± 1
Ti-K_α	4509	116 ± 1	134 ± 2
Cr-K_α	5412	118 ± 6	142 ± 4
Fe-K_α	6395	145 ± 1	164 ± 3
Cu-K_α	8040	173 ± 1	193 ± 1

Table 3: Measured energy resolution for single and all events in event mode.

Line	Energy eV	FWHM eV	
		Singles	All
Al-K_α	1486	91 ± 3	103 ± 3
Ti-K_α	4509	142 ± 16	146 ± 2
Cr-K_α	5412	142 ± 15	154 ± 2
Fe-K_α	6395	151 ± 2	176 ± 2
Cu-K_α	8040	176 ± 2	199 ± 1

4 energy shifts compared to energy-dependent CTE, 256 column-wise gains and 256 column-wise offsets per multiplicity.

In all cases, a 200 eV spectral threshold is imposed to the photon events, i.e. reconstructed patterns.

The Full Width at Half Maximum (FWHM) of the five most prominent lines are reported in Tab. 2 for full-frame operation and Tab. 3 for event mode. In the former case, results are compatible with the spectral energy resolution requirement of 80 eV at 1486 eV at the beginning of the mission. In the latter scenario, the compliance is missed and improvements are ongoing to achieve a better agreement with the mission requirements. Indeed, the mismatch of the spectral performances between the two modes of operation likely results from the different implementation of the common-mode noise correction algorithm in the FEE, as anticipated in § 3.1 and § 3.2.

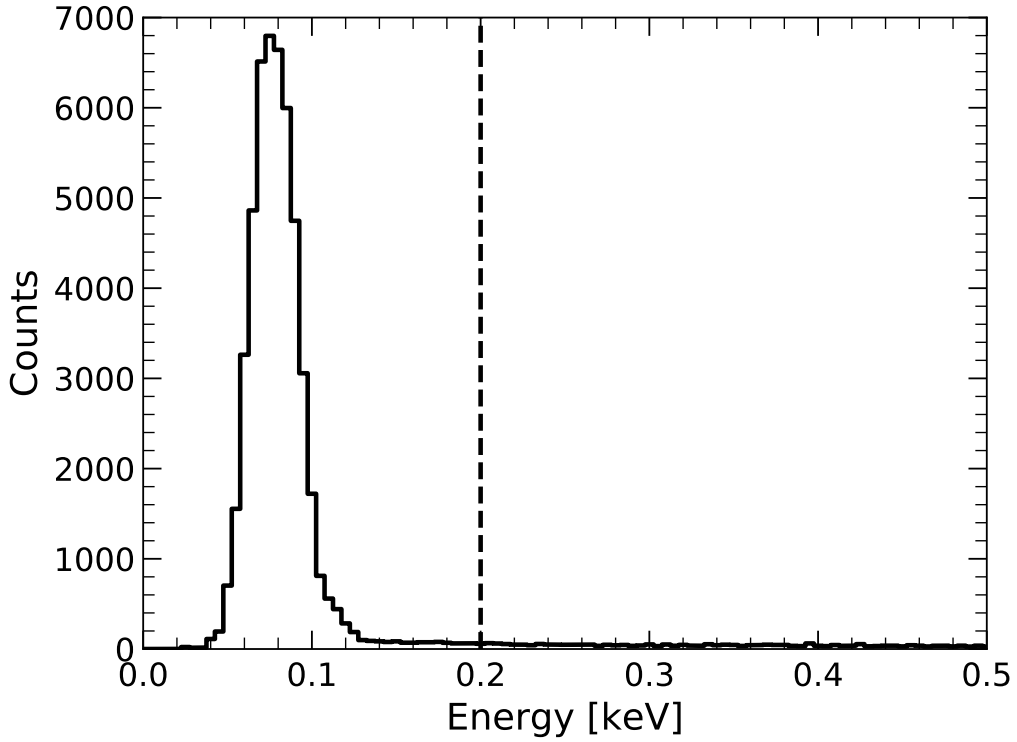

Figure 5: Low-energy portion of the single-event spectrum of Fig. 4 in case no spectral threshold is imposed. The $T = nN$ extraction threshold (with $n = 4$) of § 3.2 is still present as necessary to identify hit pixels. The instrument specification at 200 eV is marked by a dashed line.

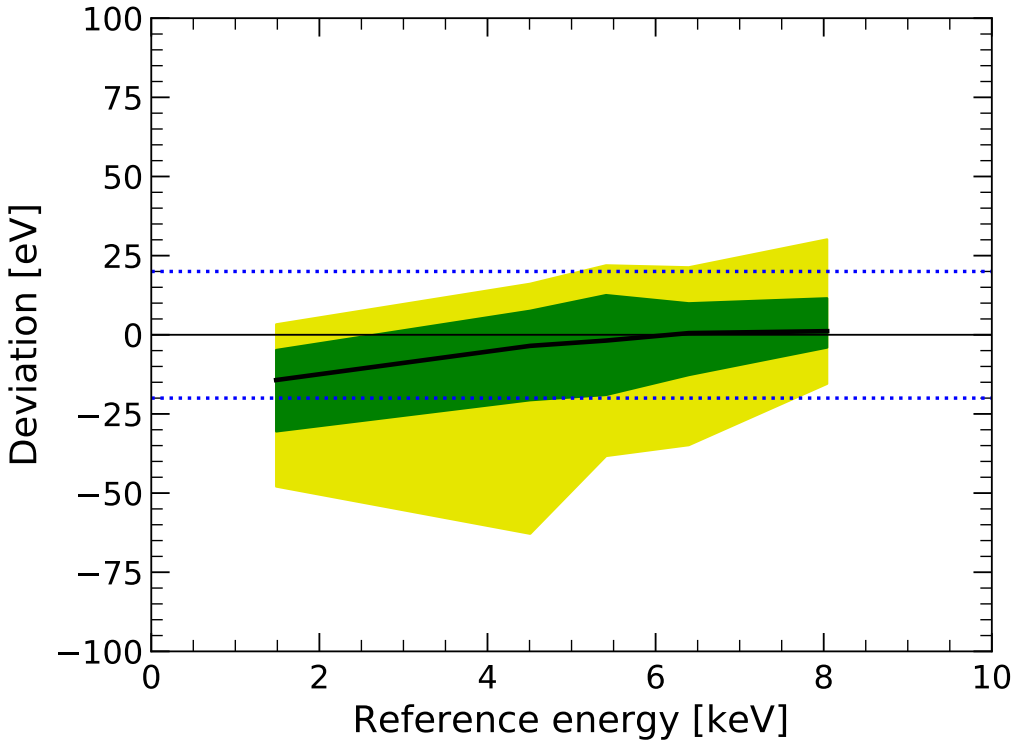

Figure 6: Distribution of the energy shifts across the columns at each reference energy. The solid black curve represents the median, while the inner (respectively outer) region indicates where 68 % (respectively 95 %) of the results lie. The dotted lines mark the ±20 eV interval.

4.4. Low-level threshold

Fig. 5 shows the < 500 eV portion of the detector-wide spectrum obtained using only single events (dotted curve of Fig. 4). Contrary to Fig. 4, in this case the 200 eV spectral threshold is not imposed and only the extraction threshold used for the identification of hit pixels (§ 3.2) is applied. The low-energy noise peak arises from spurious counts having energies above the extraction threshold, i.e. 4 times the noise level estimated from the analysis of dark frames (§ 3.2 and § 4.1). The instrument specifications require a low-energy (spectral) threshold of 200 eV, marked in Fig. 5: this is fully achieved in the case under analysis both in full-frame mode and in event mode, as the noise peak extends up to ≈ 130 eV.

Table 4: Measured Charge Transfer Inefficiency.

Line	Energy eV	CTI $\times 10^{-5}$
Al-K_α	1486	2.3 ± 0.8
Ti-K_α	4509	1.3 ± 0.2
Cr-K_α	5412	1.5 ± 0.2
Fe-K_α	6395	1.2 ± 0.1
Cu-K_α	8040	1.0 ± 0.1

4.5. Non-linearity

Fig. 6 shows the distribution across all columns of the deviations of the fitted line centers of the five main spectral lines from their respective reference energies. Median shifts are always between ±20 eV from zero and 68 % of cases are always within ±30 eV. The spread of the deviations around the median is also energy-dependent, with absolute shifts reaching 70 eV for energies around 4.5 keV.

This phenomenon is likely to be the consequence of a small channel-dependent non-linear response of the readout electronics. As the analysis algorithms are based on a linear spectral calibration, the aforementioned deviations are currently unavoidable and further studies are necessary to mitigate this effect, in relation to the requirement of < 20 eV-variations of the energy scale across the whole detector.

4.6. Charge Transfer Inefficiency

Estimates of the Charge Transfer Inefficiency at the five main spectral lines are presented in Tab. 4. The results are in agreement with the literature [5], where a value of CTI (6 keV) $= 10^{-5}$ is reported.

5. Summary and conclusions

This paper reports on the first performance tests and characterization of the detection chain of the Micro-channel X-ray Telescope on board the SVOM mission. Despite the higher operating temperature (≈ -65 °C according to the mission baseline) that sets MXT apart from previous missions mounting similar detectors, we demonstrate an energy resolution of 82 eV at 1.49 keV on the sum spectrum built with single events in full-frame mode, as well as

a $< 200\,\mathrm{eV}$ low-energy threshold, all of which show the compliance of the measurements taken in full-frame mode with the performance requirements of the instrument. Further optimization is required to decrease the mismatch between the results taken in full-frame and event modes, in order to bring the latter closer to the mission specifications. A similar care must be dedicated to the energy scale of the detector, both from a software and from a hardware point of view, in order to reduced the measured deviations.

The detector studied in this paper is currently integrated in a camera to be mounted on the Performance Model of the whole telescope for end-to-end tests at the PANTER X-ray facility.

Acknowledgements

The authors would like to thank Karine Mercier and her instrument system team at the French space agency (CNES) for their technical, quality and financial support.

This research was carried out as part of the MXT Performance Assessment study funded by CEA and CNES and in the framework of a PhD thesis funded by CEA-Irfu (CEA Saclay).

References

[1] J. Wei, B. Cordier, S. Antier, et al., The Deep and Transient Universe in the SVOM Era: New Challenges and Opportunities - Scientific prospects of the SVOM mission, arXiv e-prints (2016) arXiv:1610.06892arXiv:1610.06892.

[2] K. Mercier, F. Gonzalez, D. Götz, et al., MXT instrument on-board the French-Chinese SVOM mission, in: Space Telescopes and Instrumentation 2018: Ultraviolet to Gamma Ray, Vol. 10699 of Society of Photo-Optical Instrumentation Engineers (SPIE) Conference Series, 2018, p. 1069921. doi:10.1117/12.2313561.

[3] C. Feldman, J. Pearson, R. Willingale, et al., Testing and modelling of the SVOM MXT narrow field lobster-eye telescope, in: Proc. SPIE, Vol. 10399 of Society of Photo-Optical Instrumentation Engineers (SPIE) Conference Series, 2017, p. 103991Q. doi:10.1117/12.2273416.

[4] L. Strüder, U. Briel, K. Dennerl, et al., The European Photon Imaging Camera on XMM-Newton: The pn-CCD camera, Astron. Astrophys. 365 (2001) L18–L26. doi:10.1051/0004-6361:20000066.

[5] N. Meidinger, R. Andritschke, O. Hälker, et al., Next generation of pnCCDs for X-ray spectroscopy and imaging, Nucl. Instr. and Meth. A 568 (2006) 141–148. doi:10.1016/j.nima.2006.05.268.

[6] S. Herrmann, W. Buttler, R. Hartmann, et al., Mixed signal pnCCD readout ASIC for the future X-ray astronomy mission eROSITA, in: 2007 IEEE Nuclear Science Symposium Conference Record, Vol. 3, 2007, pp. 2398–2403. doi:10.1109/NSSMIC.2007.4436626.

[7] S. Herrmann, W. Buttler, R. Hartmann, et al., Camex readout asics for pnccds, in: 2008 IEEE Nuclear Science Symposium Conference Record, 2008, pp. 2952–2957. doi:10.1109/NSSMIC.2008.4774983.

[8] D. N. Burrows, J. E. Hill, J. A. Nousek, et al., The Swift X-Ray Telescope, in: K. A. Flanagan, O. H. W. Siegmund (Eds.), Proc. SPIE, Vol. 5165 of Society of Photo-Optical Instrumentation Engineers (SPIE) Conference Series, 2004, pp. 201–216. doi:10.1117/12.504868.

[9] E. Gatti, P. Rehak, Semiconductor drift chamber – An application of a novel charge transport scheme, Nucl. Instr. and Meth. 225 (1984) 608–614. doi:10.1016/0167-5087(84)90113-3.

[10] R. Andritschke, G. Hartner, R. Hartmann, et al., Data analysis for characterizing PNCCDS, in: 2008 IEEE Nuclear Science Symposium Conference Record, 2008, pp. 2166–2172. doi:10.1109/NSSMIC.2008.4774781.

[11] I. Valtchanov, M. Smith, N. Schartel, XMM-SOC-CAL-SRN-0367, EPIC-pn Energy Scale for Large Window Mode: long-term CTI and pattern corrections (2019).